Imaging and quantification of the tumor microenvironment of triple negative breast cancer using TPEF and scanning laser optical tomography

HANNES KAMIN,[1,*] ⓘ LENA NOLTE,[1] ANDREAS BLEILEVENS,[2] ELMAR STICKELER,[2] DAG HEINEMANN,[1,3,4] JOCHEN MAURER,[2] SONJA JOHANNSMEIER,[1,5] ⓘ AND TAMMO RIPKEN[1,5]

[1]*Industrial and Biomedical Optics Department, Laser Zentrum Hannover e.V., Hollerithallee 8, 30419 Hannover, Germany*
[2]*Clinic for Gynecology and Obstetrics, University Hospital Aachen, Pauwelstr. 30, 52074 Aachen, Germany*
[3]*Department of Phytophotonics, Institute of Horticultural Production Systems, Leibniz University Hannover, Herrenhäuser Str. 2, 30419 Hannover, Germany*
[4]*Hannover Centre for Optical Technologies (HOT), Leibniz University Hannover, Nienburger Str. 17, 30167 Hannover, Germany*
[5]*Lower Saxony Centre for Biomedical Engineering, Implant Research and Development, Stadtfelddamm 34, 30625 Hannover, Germany*
[*]*h.kamin@lzh.de*

Abstract: Triple-negative breast cancer is an aggressive subtype of breast cancer that has a poor five-year survival rate. The tumor's extracellular matrix is a major compartment of its microenvironment and influences the proliferation, migration and the formation of metastases. The study of such dependencies requires methods to analyze the tumor matrix in its native form. In this work, the limits of SHG-microscopy, namely limited penetration depth, sample size and specificity, are addressed by correlative three-dimensional imaging. We present the combination of scanning laser optical tomography (SLOT) and multiphoton microscopy, to depict the matrix collagen on different scales. Both methods can be used complementarily to generate full-volume views and allow for in-depth analysis. Additionally, we explore the use of SHG as a contrast mechanism for complex samples in SLOT. It was possible to depict the overall collagen structure and specific fibers using marker free imaging on different scales. An appropriate sample preparation enables the fixation of the structures while simultaneously conserving the fluorescence of antibody staining. We find that SHG is a suitable contrast mechanism to depict matrix collagen even in complex samples and using SLOT. The insights presented here shall further facilitate the study of the tumor extracellular matrix by correlative 3d imaging.

1. Introduction

The triple-negative breast cancer (TNBC) is both aggressive and difficult to treat. The tumor cells lack expression of surface receptors that represent the targets for many types of hormone therapy [1]. Consequently, there exists a demand for alternative treatment strategies. Current research strongly suggests that apart from cellular characteristics, the properties of the extracellular matrix (ECM) play a critical role for cell adhesion, proliferation and migration of the tumor [2]. It constitutes a crucial part of the tumor stem cell's microenvironment. The ECM is a three-dimensional network consisting of macromolecules and minerals such as collagen, glycoproteins or hydroxyapatite. Its various functions include providing structural support to surrounding cells, cell adhesion and cell-to-cell communication. The cancerous ECM is different from that of native tissue: it is remodeled during tumorigenesis and is characterized by stiffer mechanics

and increased collagen production [3]. An influence on the efficiency of anti-tumor drugs has been suggested as well [4]. In spite of its crucial role, the cancerous ECM is rarely considered during the development of new therapies, nor do the cancer cell lines adequately represent the heterogeneity of the TNBC patients [5]. An understanding of the tumor's ECM architecture and its inter-patient variability is crucial to perform effective research in the identification of target structures and the development of therapeutics.

Adequate imaging methods are required to assess a tissue's collagen architecture. Each method operates within a specific size range (e.g. *cm* scale for optical coherence tomography to *µm* scale for two-photon excitation fluorescence microscopy (TPEF)). To include both a structural overview and a detailed analysis of a chosen region of interest (ROI), multiple compatible methods need to be combined. The ideal method would forego any alterations or artefacts that arise from external staining such as limited penetration depth of antibodies in large samples. Therefore, marker-free methods to visualize collagen, such as second harmonic generation (SHG), might be favorable. The non-centrosymmetric collagen fibers are known to generate an SHG signal [6] which is used as an inherent contrast mechanism in biomedical imaging. However, most studies use thin tissue slices or suffer from the limited penetration depth of TPEF. In this study, a maximum penetration depth of approx. $400 - 500\,\mu m$ depending on the optical clearing was obtained, which is in agreement with most imaging studies according to literature [7]. Furthermore SHG microscopy only obtains *en face* sections and therefore does not detect fibers which are orientated parallel to the optical axis. Since, a structural overview of the sample's collagen distribution on the millimeter or even centimeter scale cannot be generated this way which in turn is desirable for many samples such as cancer as it would greatly improve and complete the information gained by SHG-imaging [8].

Scanning laser optical tomography (SLOT) [9], a light-based tomographic technique, was developed from the basic principles of optical projection tomography (OPT). It allows for non-destructive light-based tomographic imaging of tissue samples of up to a cubic centimeter in size. During a complete SLOT-measurement the sample is rotated around itself and thus the fiber orientation is constantly changed towards the polarization of the incoming laser beam. Since the SHG-signal is strongly dependent on the orientation, the underlying physical process of SHG limits the imaging sample due to inconsistent signal strength. Recently however, the use of SHG as a contrast mechanism for SLOT has been demonstrated in theory and with simple collagen structures [10] by defining the dependence between orientation of the fibers and the polarization of the incident light, suggesting that SHG imaging of a rotating sample should be possible with linearly polarized light and a polarization angle of $\alpha = 0°$. The combination of this tomographic technique and a high resolution method such as TPEF would allow for great advantages in the evaluation of a tumor's collagen architecture. This work presents protocols and results of TNBC-tumor preparation and imaging using two contrast mechanisms (antibody staining and SHG) in two different imaging setups (SLOT and TPEF). It constitutes a proof of concept for the use of SHG to image large samples with complex collagen structures. Within the context of SLOT, the dependence of SHG intensity on laser polarization (linear vs. circular) was found to be neglectable, contrary to expectations [11]. A protocol for optical clearing and sample embedding is presented that allows for antibody-based fluorescence imaging as well as SHG imaging of the same sample. The combination of these methods allows for a thorough comparison of multiple tumor samples and reveals their characteristic differences. Furthermore, approaches to quantify the data, the respective preprocessing steps and appropriate visualization of the cancer samples are demonstrated to complete the entire examination process.

2. Methodology

2.1. Tumor preparation

Patients were operated in the Department of Gynecology and Obstetrics at the University Clinic RWTH Aachen. Tumor tissue was macroscopically examined by a pathologist of the RWTH centralized Biomaterial Bank. Tumor pieces for further investigations were either fixed with 4% formaldehyde at least for 24 *h* or snap frozen with liquid nitrogen. Pieces for primary cell culture were processed further as described in [12]. Fixed samples were shipped at room temperature to the Industrial and Biomedical Optics Department in Hannover.

2.2. Sample preparation for 3D imaging

All tumors were fixed in 4 % formaldehyde solution for 24 *h*. Following fixation, optical clearing was performed to enable in-depth optical imaging of the tumor samples. During this process, the refractive index of the liquid components was adjusted to that of the solid compartments. A homogeneous refractive index would then allow the light to propagate through the sample without being scattered uncontrollably, thereby allowing for reliable tomographic image reconstruction. As a target refractive index for optical clearing, $n = 1.56$ in agreement with other standard clearing methods as *3DISCO* or simple immersion with benzylalcohol / benzylbenzoate (BABB). Prior to the actual clearing process, this target refractive index was varified using simple immersion clearing with BABB and ethylciannamate ($n = 1.56$ for both). The samples were dehydrated with an ethanol series of ascending concentration (50 %, 70 %, 100 %, 100 %, one hour each). Subsequently the samples were immersed ECI and BABB (Fig. 4). The following samples were prepared for imaging according to a previously developed method for embedding and clearing biological samples: Curing Resin-Infiltrated Sample for Transparent Analysis with Light (CRISTAL) [13]. These samples were dehydrated as described above. The ethanol was then replaced by benzyl alcohol (100 %, twice for 30 min each) before the samples were infiltrated by an optical adhesive with the defined refractive index of $n = 1.56$ (NOA 71; Norland Products Inc., USA) for 12 h. The samples were transferred to a PTFE hose and irradiated with UV light (360 *nm*) for 90 minutes at $4°C$. The cured sample could then be removed from the hose and mounted in the imaging setups. To evaluate the quality of marker-free collagen imaging and to increase the specificity, antibody staining of collagen I fibers was performed as well. Fixated samples (approximately $3 - 4 \ mm^3$ in size) were washed three times in PBS (2*h* each) and then incubated for 9 days in the primary antibody solution (20 $\mu g/ml$ rabbit anti-collagen type I (Rockland, USA) in PBS + 1 % BSA). A goat anti-rabbit-Cy3 conjugate (4 $\mu g/ml$ in PBS + 1 % BSA; excitation max: 554 *nm*, emission max: 558-574 *nm*; Elabscience, China) was chosen as secondary antibody with an incubation time of 9 days. The samples were washed in PBS three times, 2 *h* each, between and after staining steps. Then, dehydration, clearing and embedding followed as described above.

2.3. Scanning laser optical tomography (SLOT)

Scanning Laser Optical Tomography (SLOT) is a technology developed at the *Laser Zentrum Hannover e.V.* and is based on the principle of computed tomography. However, instead of X-rays, SLOT uses laser beams as excitation source. It can be used to acquire mesoscale, non-destructive three-dimensional image data. Two different SLOT-setups (referred to as micro-SLOT and macro-SLOT, respectively) were used in this study. SHG was excited in the micro-SLOT with a femtosecond laser (Chameleon Ultra II; Coherent, USA) at 980 *nm* and collected in forward direction. Linear polarization with a rotation angle of $\alpha = 0°$ relative to the rotation axis of the sample was realized with a $\frac{\lambda}{2}$ plate. During parameter testing, circularly polarized light was generated by an additional $\frac{\lambda}{4}$ plate inserted in front of the scanner. The embedded tumor samples were submerged in a cuvette containing silicone oil with a refractive index matched to that of the

cleared sample. The beam diameter was adjusted with a variable optical beam expander ($0.5x$ – $2x$; Thorlabs, USA) to $3 - 5\,mm$ depending on the sample size, where larger samples demanded a smaller beam diameter. By the adjustment of the beam diameter, the length of the excitation point spread function covers the full thickness of the sample [10]. The sample was rotated by $360°$, and 1200 projections of the scans were recorded at equidistant angles with an integration time of $5\,s$ per projection and optical power of $583\,mW$. For one projection image, the sample was scannend in a meandering pattern and the intensities were recorded pointwise, shown in Fig. 2. A photomultiplier tube (PMT) collected the emitted light on the opposite site, with filters blocking the excitation light from the SHG signal (Fig. 1(a)).
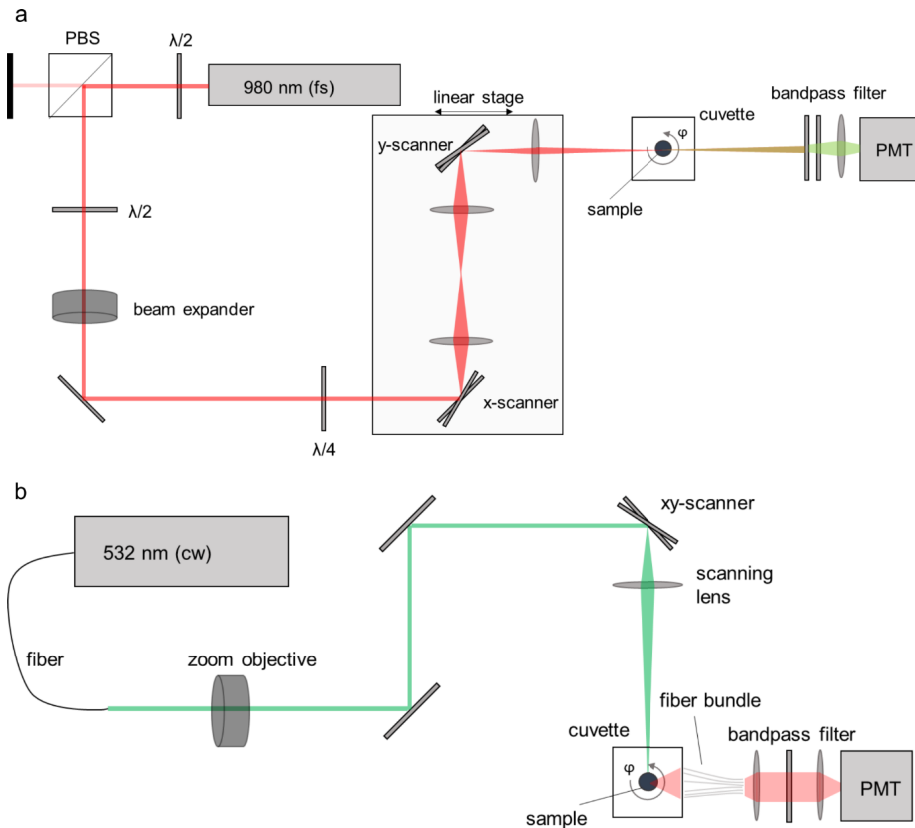
Fig. 1. SLOT- setups. Micro-SLOT (a) for forward SHG collection. The beam of a femtosecond- laser is scanned across a rotating sample which is placed inside a cuvette. A PMT collects the emitted light that passes through the bandpass filter. The $\frac{\lambda}{4}$ plate was used to create circular polarization and removed when linear polarization was used. A polarizing beam splitter (PBS) in combination with a rotatable $\frac{\lambda}{2}$ plate was used to set the laser excitation power. (b) Macro-SLOT for fluorescence detection. Visible light is provided via a fiber, and the light emitted by the sample is collected by a fiber bundle and guided onto a PMT.

The macro-SLOT was used to record fluorescence of stained samples. A laser diode ($532\,nm$) was coupled to a single-mode fiber and the beam diameter was adjusted with a zoom objective ($6x$). A scanning lens was positioned at a variable distance from the sample plane to ensure a stable focal plane if various wavelengths are used. A fiber bundle collected the emitted fluorescence light and guided it onto a PMT, where a bandpass filter (578/16) selected the emission wavelengths of Cy3 (Figure 1(b)).
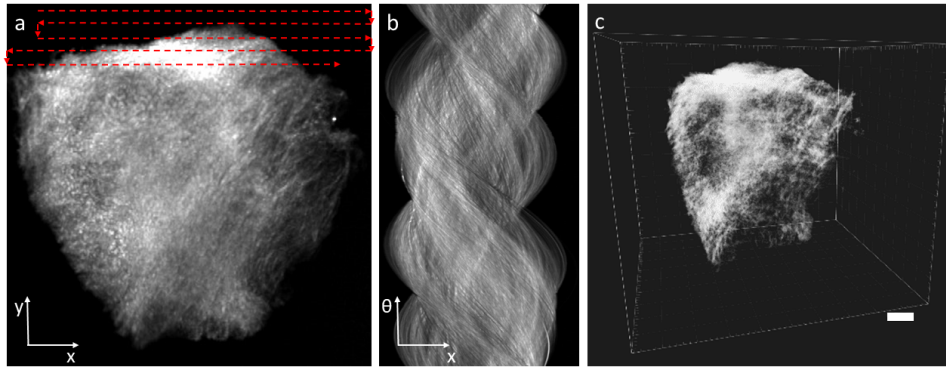
Fig. 2. Reconstruction of SLOT projection images. Projection-image (a) of TNBC sample. The sample was scanned in meandering pattern and SHG emission is collected in formward direction. (b) All projection images are transformed into sinograms and subsequently reconstructed to obtain the volume of the sample using the FBP (c). Scale bar is 200 μm.

2.4. Two-photon excitation microscopy

Two-photon excitation microscopy was performed with the upright modality of the TriM Scope II "Horizontal" (LaVision BioTec, Germany) and the same femtosecond laser as used in the micro-SLOT. The wavelength of the laser source can be adjusted in range of 680 $nm(>650\,mW)$ to 1080 $nm(>200\,mW)$. The cured samples were polished to expose the tumor to the edge of the NOA polymer block. The samples were excited with the fs-laser through a 20x objective, and the laser light was scanned across the sample surface. Emitted light was collected in backwards direction by the objective and guided to one of two photomultiplier tubes (PMTs). A dichroic mirror with a cut-off wavelength of 495 nm reflected the SHG signal (λ_{em}<495 nm) to PMT1, while antibody fluorescence (λ_{em}>495 nm) was detected by PMT2. To increase specificity of the detected signals, bandpass filters were placed in front of the PMTs (500/20 for PMT1, 565/24 for PMT2). The excitation wavelengths were λ_{ex} = 980 nm for SHG and λ_{ex} = 1040 nm for antibody imaging. Each scanning image had a size of 450 μm x 450 μm, and larger areas were stitched together from multiple mosaic images using the Fiji [14] plugin 3D stitching [15]. Z-planes were recorded with a distance of 2 μm.

2.5. Reconstruction of image data

SLOT-data was reconstructed with a custom Fiji macro, based on the open source package IMOD [16]. Raw data was recorded as a sinogram, and the reconstructed images were obtained via filtered back projection (FBP). Also, the macro improved the contrast of the PMT signals and corrected tilting of the sample axis. SLOT-SHG images were corrected by calculating the square root of the intensity of each pixel. This operation was performed to account for the quadratic dependence of the SHG signal strength on the number of scatterers N ($WSHG \propto N^2$), which in turn varies with sample thickness. Although this dependence is confined to the coherence length of SHG where phase matching occurs, a previous study showed that quasi phase matching can be assumed for the present imaging geometry and a linear dependence of the SHG signal can be achieved ($\sqrt{WSHG} \propto N$) [10]. Thus, this operation was performed on reconstructed SLOT-SHG images.
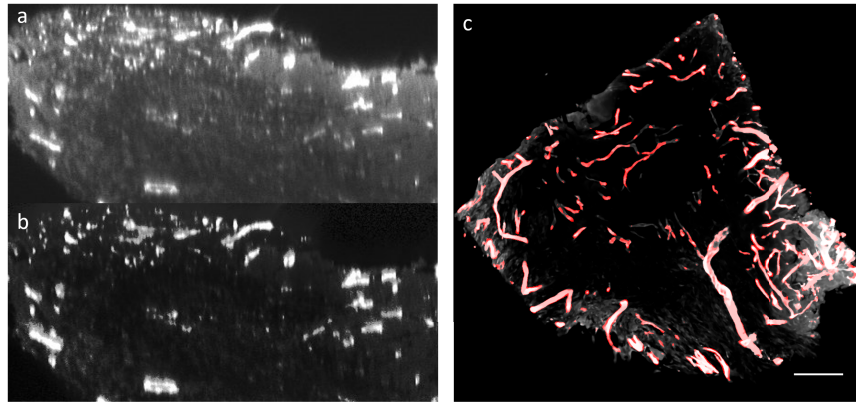
Fig. 3. Equalization of fluorescence intensity and segmentation of vessels. (a) Intensity of the stack in zx-plane. (b) Intensity of the stack in zx-plane after the intensity correction and histogram equalization showing that the ratio of fluorophore and background emission is enhanced. (c) Segmentation of vessels with the Random Forest Algorithm (original image data in greyscale and segmented structures in red). Scale bar is 200 μm.

2.6. Orientation analysis of TPEF image stacks

To gain further information on the tumor microenvironment, the three-dimensional orientation of the collagen fibers and the blood vessels were quantified. Two different approaches have been chosen, one analyzing the fibers revealed by SHG and another examining the fluorescence data. Since the SHG – data revealed dense fiber networks and thus prohibited individual segmentation and subsequent analysis in 3D, the collagen fiber network was examined in 2D using a Maximum Intensity Projection (MIP). Then the ImageJ plugin OrientationJ [17] which is based on the evaluation of the local gradient structure tensor was used to represent the orientation of the fibers in a hsv colormap.

The antibody staining revealed vessels as a clear network that was found suitable for individual vessel analysis. In order to quantify and visualize the orientation of the vessels, a fiber extraction algorithm was used that is based on the Fiber Extraction Algorithm (FIRE) originally developed by Andrew M. Stein [18]. The FIRE-Algorithm is an automated tracking algorithm that enables individual analysis of single fiber like structures by extracting their three-dimensional geometry. The procedure has been adapted over the past decade i.e. applying a curvelet filter in the preprocessing step [19] and has become a validated method to examine the collagen structure in breast cancer [20]. Summarizing the method, the image is segmented such that the fibers represent the foreground pixels. A distance map is applied to the binary image so that the foreground pixels yield their distance to the background. Then, after smoothing the image, "seedpoints" are identified which represent local maxima of the distance map. From these seedpoints, branches are formed by following the maximum intensities along the fiber center (distance map). After combining the fiber skeleton points, the resulting fiber network is reworked by pruning, linking or deleting certain fibers according to their lengths, directions and arrangements. In this work, the tracking algorithm was rewritten in python based on [18] with some adaptations including the preprocessing and segmentation process. Since this algorithm was originally invented to analyze collagen in hydrogels which differs heavily from tnbc-samples, some preprocessing adaptations have been made. To begin with, the images have been denoised by the "Anisotropic Diffusion" algorithm. As expected, the fluorescence intensity decreases towards deeper sections of the tissue. *Intensify3D*, a programm described in [21], has been used to address this common problem and to balance the pixel intensities along the z-axis. Briefly, the fluorescence intensity is

equalized in xy and z direction by division of the original image with a generated background mask and subsequent stretching of the contrast along all slices in z direction (Fig. 3(a)). Then, the background was subtracted by the rolling ball algorithm and segmented by the *Weka Trainable Segmentation Tool* [22].

For this purpose, the image was labeled with three different classes, i.e. background, background fluorescence and fiber. The resulting fibers of the FIRE Algorithm were analyzed regarding their three-dimensional orientation. A single fiber was separated into groups of their skeleton points which can be fitted with a straight line and thus represent the direction of that fiber section. The fiber network was visualized with the python plugin quanfima [23]. The direction is shown in the hsv color space where horizontal direction is shown with the color and the vertical direction in saturation of the color.

3. Results

3.1. Optical clearing and embedding of the tumor samples

To obtain optically clear samples and avoid scattering artifacts during 3D imaging, the refractive index match was tested before producing cured samples. Both of the clearing solvents BABB and ECI yielded good results. The target refractive index for subsequently cleared and cured samples for imaging was therefore set to $n = 1.560$. The polymer NOA 71 possesses this refractive index, and was therefore used during the CRISTAL process. The fluorescence signal of the conjugated antibody was preserved for several weeks after curing and the samples could be successfully embedded in an optically cleared rigid cylinder (Fig. 4). Thus, reproducible measurements in both SLOT-setups and TPEF were possible.
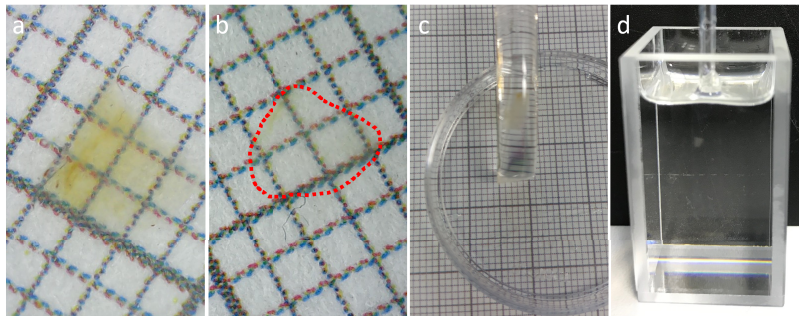

Fig. 4. Clearing and embedding of TNBC samples. Clearing of the samples using (a) ECI (refractive index $n = 1.56$) and (b) BABB (red line indicates the edge of the sample) showed transparent and clear results hence determining the target refractive index. Optically cleared and embedded sample in a rigid cylinder (c) for reproducible measurements with SLOT and TPEF. (d) Embedded sample in cuvette with refractive index matched silicon oil.

### 3.2. Influence of laser polarization on SHG imaging in SLOT

As SHG imaging of complex collagen networks using optical projection tomography had not been demonstrated before, the dependence of signal intensity on power and polarization was investigated. The laser light was polarized either linearly ($\alpha = 0°$) or circularly with different power settings, and projection images were generated as described in Section 2.5. from the same randomly selected sample with all settings. The signal intensity was evaluated along two randomly selected lines (Fig. 5(a)) of measurements of the same Field of View with different settings (polarization and laser power). Raw intensities were corrected by taking the square root for each pixel, and then normalized to the respective maximum value (Fig. 5(c-h)) to take

into account the quadratic dependance on the number of scatterers. It was apparent that all settings yielded qualitatively similar images that mostly differed in intensity. The obtained SHG signal was stronger for linearly polarized light. The influence of the parameters was evaluated for a complete 360° rotation as well using linear (583 *mW*) and circular (831 *mW*) polarization (Fig. 5(i, j)). The corrected intensity was summed up along one randomly selected line which was perpendicular to the rotation axis of the sample (Fig. 5(b)) and then normalized to the
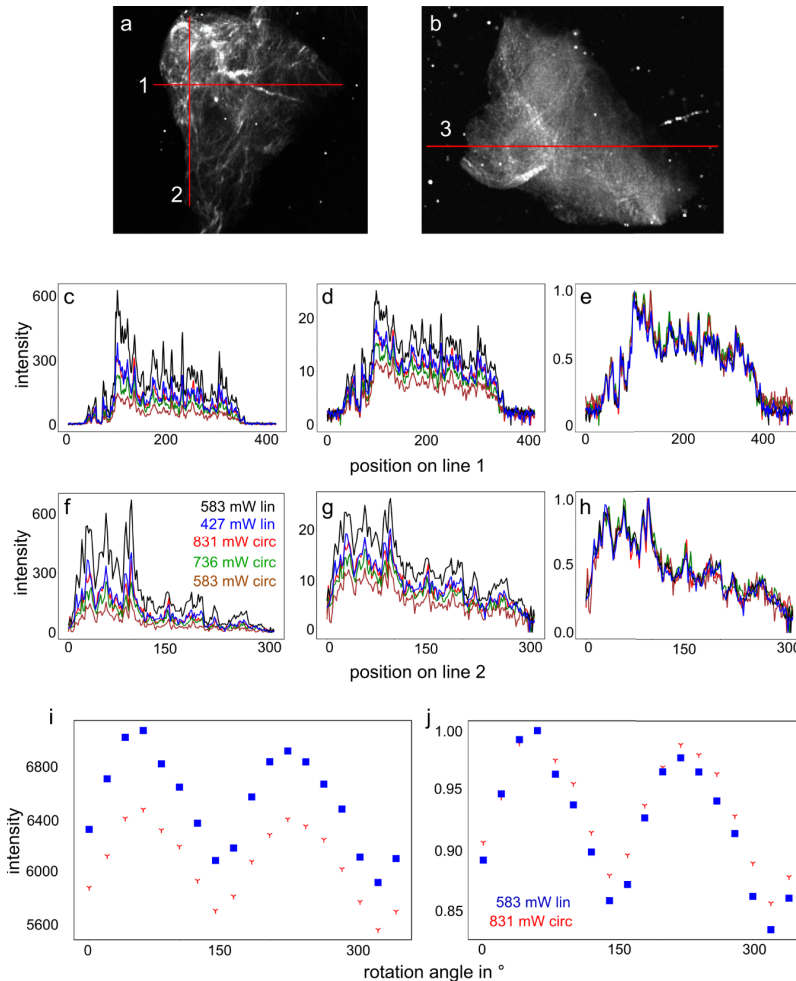

Fig. 5. Influence of the laser polarization on the SHG-signal. Results show the influence of the polarization and power of the excitation laser on the SHG intensity for one projection (a, c-h). Also, the SHG intensity for a full measurement namely projections over the range of 360 degrees with linear and circular polarized light is shown (b, i, j). (a) SHG intensity was compared along the two lines denoted in the still image. (b) SHG intensity was summed up along the red line for a full sample rotation to examine the SHG intensity for a full rotation. (c-e) SHG intensity along line 1 (a) before (c) and after (d) taking the square root of each pixel, and after subsequent normalization (e). The emitted intensity is strongest for linearly polarized light (c, d). The qualitative comparison shows no clear distinction between the different polarizations (e). (f-h) The same procedure along line 2 (a). (i, j) The summed SHG intensity fluctuated periodically with approximately half a rotation. Again, this was observed independently of laser polarization (j).
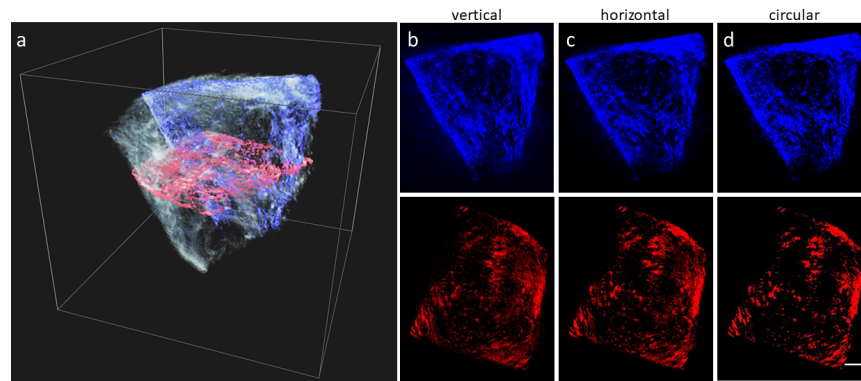
Fig. 6. Reconstruction of SHG-projection images with different laser polarizations. (a) View of the whole sample with highlighted planes in xy and zy direction used for qualitative analysis. (b-d) MIP of five planes of highlighted planes and locations with different polarizations. Only minor differences due to laser polarizations can be determined. Scale bar is 200 μm.
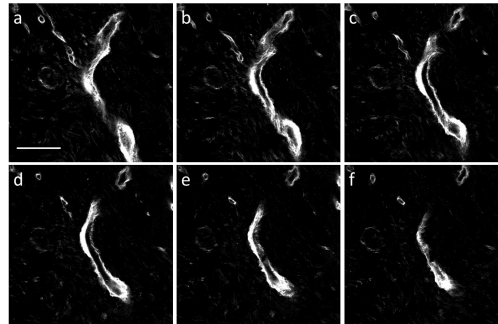

Fig. 7. Antibody staining revealing vascular structures. Exemplary vessel in different slices of z-stack (a-f). The distance between the slices is 8 μm. Scale bar is 100 μm.

respective maximum. An optimal measurement would yield the same sum of intensities for a line perpendicular to the rotation axis for all projections directions. The emitted intensity was again higher for linear polarization. However, both settings yielded intensity profiles that fluctuated nearly periodically with the rotation angle (Fig. 5(i-j)). Two maxima were detected approx. 180° apart.

To further examine the influence of the laser polarization on the SHG intensities in the resulting reconstructed image, further samples were imaged and reconstructed as described and investigated qualitatively. Circularly, horizontally and vertically polarized light with equal intensity of 583 mW was used. Two perpendicular planes, the xy and the zy plane, were chosen to access the information on the collagen distribution within the sample. A maximum intensity projection of 5 planes was obtained. The results are shown in Fig. 6 and demonstrate that the incoming laser polarization (horizontal, vertical and circular) in combination with the signal correction steps as described in the previous section has only a minor influence on the structures revealed by SHG-SLOT. For subsequent imaging, linear vertical polarization at 583 mW was used.
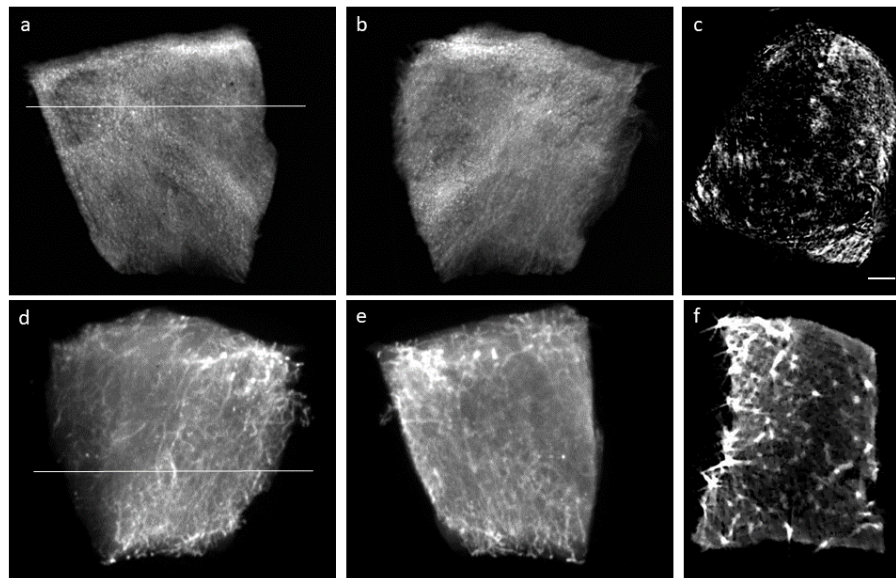
Fig. 8. Comparison of different contrast mechanisms of SLOT. (a-c) Second Harmonic Generation revealing the collagen distribution. Two different exemplary projections (a,b) recorded in the micro-SLOT are shown. (c) Reconstructed slice revealing the distribution of collagen within the sample. (d-f) Antibody staining showing the vessel structures. Two exemplary projections (d,e) recorded in the macro-SLOT are shown. (f) Reconstructed slice. The fluorescence intensities vary according to their distance to the edge of the sample. Scale bar is 200 μm.

3.3. Antibody staining

The antibody used here was specific for collagen 1, yet the structures that were marked by the staining process clearly vascular structures, likely by binding to the vascular collagen (Fig. 7) as collagen type 1 is among the most commonly found collagen types within the media and adventitia of the vascular wall [24].

Antibody staining yielded strong fluorescence near the surface of the samples. The reconstructed slices from the SLOT-fluorescence data revealed structures crossing through the entire sample volume (Fig. 8) although fluorescence intensities decreased towards the center. Thereby a comparison of the distribution of the vessels and the collagen of the ECM could be obtained. The distribution of the structures mainly differed in their density and orientation. The main limitation of antibody staining of 3D volumes remained the limited penetration depth of the fluorescent probes. This was obvious in comparisons with samples that had undergone shorter incubations times with the antibodies (not shown). A comparison of the two contrast mechanisms – SHG and fluorescence – in SLOT is shown in Fig. 8 where two exemplary projections and the reconstructions are depicted.

3.4. Two-photon excitation microscopy

The use of both contrast mechanisms was compared with the higher resolution of TPEF. Here, SHG and antibody fluorescence could be excited from the same locations, allowing for direct mapping of the collagen structures. An overview of the revealed structure is shown in Fig. 9. Detailed analysis with TPEF was performed on an ROI that was selected from the overview generated with fluorescence-SLOT. Composite images were created by overlaying fluorescence and SHG signals from TPEF (Fig. 9(d)) as well as combining SHG signals from TPEF with
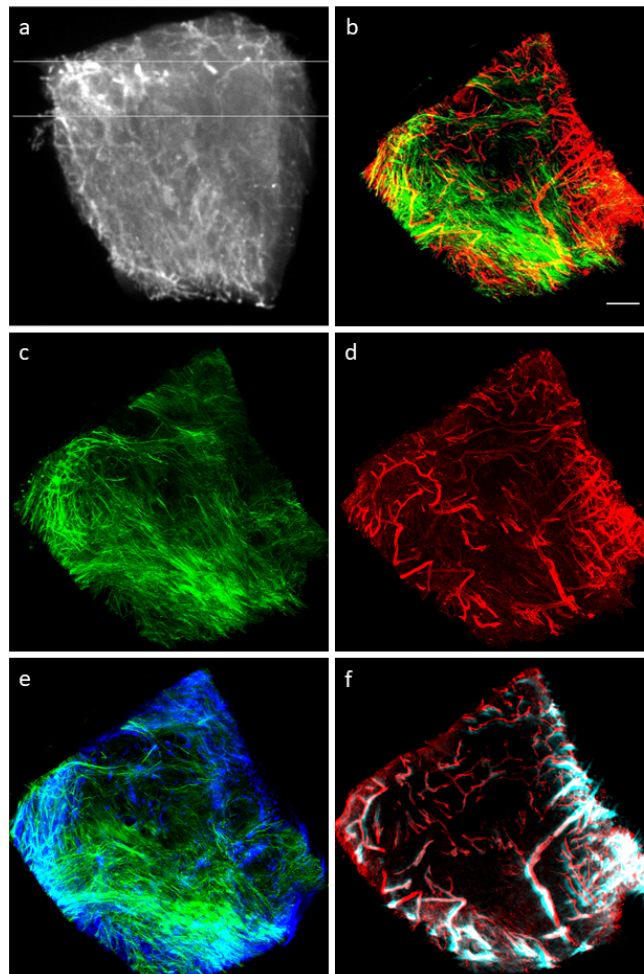
Fig. 9. Two-photon excitation microscopy reveals details of the vessel and collagen alignment. (a) Overview of the whole sample generated with SLOT. The upper segment (between the two white lines) was chosen as ROI and analysed with TPEF. (b) Maximum Intensity Projection of Collagen (green, SHG) and blood vessels (red, fluorescence) within the ROI. (c) Collagen fiber network (SHG). (d) Blood vessels revealed by antibody fluorescence. (e) Overlay of SHG-imaging of collagen revealed by SLOT (blue) and TPEF (green) within the ROI. (f) Overlay of fluorescence data acquired with SLOT (cyan) and TPEF (red).

SLOT (Fig. 9(c)) and fluorescence images from TPEF with SLOT (Fig. 9(f)). Composite images show that the fluorescence signal of the TPEF and SLOT data matches well, with exceptions of small structures that could only be revealed by TPEF. The SHG data exhibits significant differences (Fig. 9(e)). The resolution of TPEF is substantially higher and therefore revealed individual fibers, while the SLOT data only represents a general distribution of the collagen.

3.5.   Advanced analysis and visualization of TPEF data

To gain further insights on the collagen distribution and vessel alignments, the TPEF data was processed as described in chapter 3. The registered and merged TPEF data is shown as rendered 3D data in Fig. 10 (top). This overview already signals strong fibrosis that can be recognized based on the dense fiber networks revealed by SHG (Fig. 10(a), green). The subsequent analysis
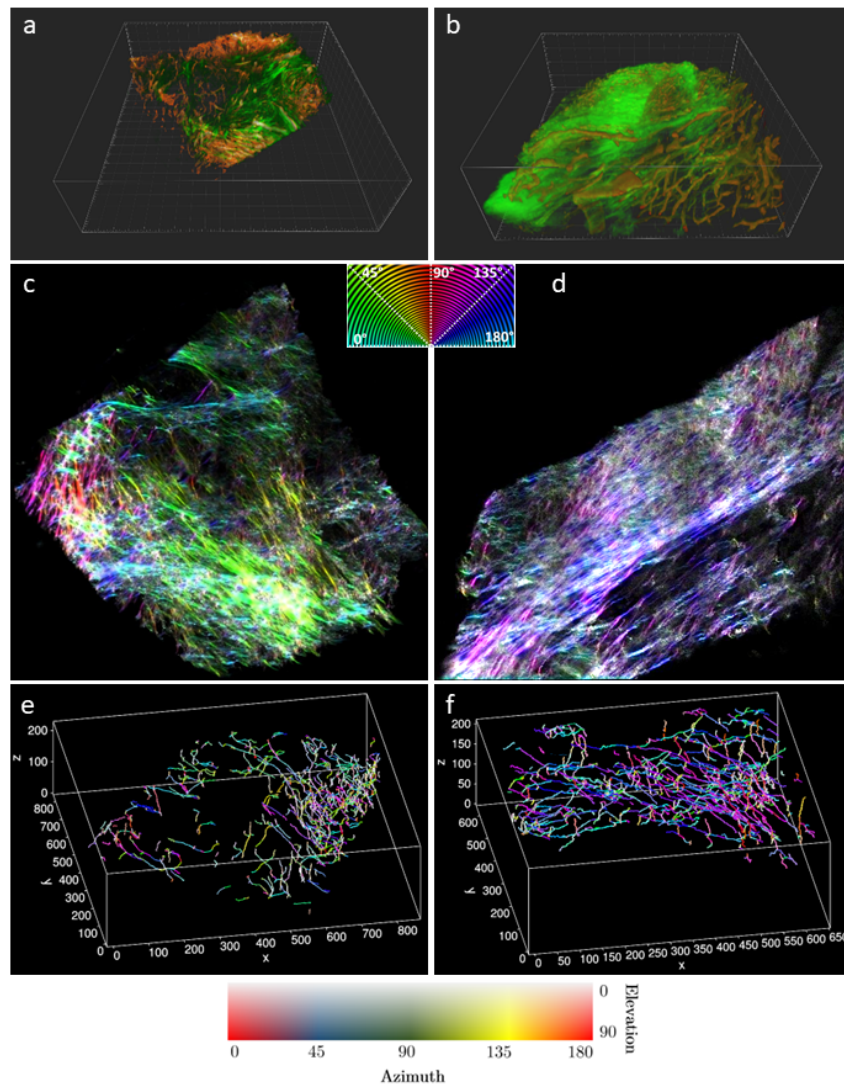
Fig. 10. **Advanced analysis of vascular structures and collagen orientation.** Two different samples (a and b) recorded with TPEF are analyzed. (a, b) 3D rendering of collagen (green) and blood vessels (red). (c,d) Maximum intensity projection of SHG image stack and orientation analysis performed with OrientationJ. Orientation of fibers can be obtained from color bar (based on the test image of the plugin). (e,f) Resulting vascular network network extracted with the adapted fiber extraction algorithm. The orientation of the 3D blood vessels is displayed via hsv color space. The color represents azimuth of the vessel in horizontal plane and the brightness describes the elevation.

of the orientation reveals highly aligned and dense fibers. Within some areas, a predominant direction can be determined, giving an indication for evidence of the matrix remodeling process. The right sample shows virtually only one predominant fiber direction, while the orientations of the fibers of the left sample are more homogeneously distributed. Hence, this method reveals significant quantifiable information. The vessels are analyzed with the fiber extraction algorithm and the result of their orientation is visualized in Fig. 10(e-f).

4. Discussion

This work shows the potential of combining 3D imaging methods on different size scales using two different contrast mechanisms. The collagen architecture of the entire tumor volumes of several millimeters in size was successfully revealed by projection tomography, and in depth-analysis was possible with two-photon excitation microscopy. The complementary use of TPEF and SLOT allows for thorough comparative top-down analyses on the same sample. The results show that second harmonic generation can be exploited to reconstruct an image of a rotating sample with a complex collagen network in projection tomography and therefore present an alternative to the work of *Campbell et al.*[25]. The main benefits of SLOT are that samples of several millimeters can be analysed and the modular setup allows the integration of further detection channels using absorption, scattering and fluorescence (1P and 2P). Furthermore, complementary analysis using SLOT and TPEF is shown. It has to be noted though that the approach used [25] is faster and direction analysis of the SHG-signal (forward / backward) is possible.

This work extends the previously published simulations and initial experiments of SHG-SLOT [10], which suggested strong intensity fluctuations depending on the orientation of the collagen fiber and the polarization of the excitation beam. The comparison between SHG and fluorescence imaging shows that the emitted SHG signal is suitable to reconstruct dense collagen networks with unpredictable fiber orientation. Simulations from [10] suggested that this should be achievable with a polarization angle of $\alpha = 0°$ relative to the rotation axis of the sample. Other sources [26] predict a strong dependence of the SHG intensity on laser polarization as well. This was however not observed when comparing linear and circular polarization (Fig. 5). In the SLOT setup, the elongated focus covers multiple collagen fibers of different orientations in a dense network such as the samples investigated here. Possibly, this has an equalizing effect on the emitted SHG intensity within the resolution limits of the SLOT. The fiber density in the samples investigated here might be too high, introducing too much complexity to be captured by the previously performed simulations. Both the imaging setup, including post-processing, and the sample characteristics presented here exceed the complexity of those described in the earlier studies. The present study demonstrates that an excitation beam with either linear polarization ($\alpha = 0°$) or circular polarization can be used to obtain marker-free three-dimensional reconstructions of a collagen network in tumor tissue. Slow intensity fluctuations of the SHG signal were observed during a full rotation of the sample. This effect has not been observed during fluorescence imaging (data not shown). The distance that the laser travels through the non-linear medium of a collagen fiber changes during sample rotation and the resulting intensity changes are encountered by taking the square root of every projection. Preparation artifacts might become visible here as well. These effects are inherent to the sample geometry. A more sophisticated correction algorithm would have to be developed to compensate for such artifacts caused by sample rotation. Although the Rayleigh length was adjusted to the length of the sample to enable uniform excitation of the fluorophores and generation of SHG signal, the intensity of the exciting beam has to be further examined when penetrating the sample. The SLOT-data presented here can therefore not be used to draw quantitative conclusions from the SHG intensity for single fibers, but rather presents qualitative overviews of the tumor samples.

A protocol to combine antibody staining with rigid refractive index-matched embedding of tissue samples has been demonstrated. The fluorescence of the Cy3-label was preserved by the CRISTAL method, and fluorescence was detectable for at least five weeks after embedding. A long incubation time is necessary to stain the deeper layers of tissue samples; in the protocol presented here, vessels in the sample's core were stained but the overall intensity decreased towards the center. TPEF imaging revealed that SHG and antibody staining did not necessarily depict the same fiber structure. The predominant collagen type in the tumor samples was expected to be type I [3]. SHG is however emitted from various collagen types (mainly types I and II [27]). It has to be noted that the SHG signal could only be detected in backwards direction in

the TPEF setup so depending on the fiber structure the recorded intensities might lack some information. After examining the first images, it was clear that the staining protocol used within this work marked the blood vessels rather than collagen fibers. One possible explanation is that the antibodies bind to the collagen found in the epithelial tissue. Diffusion might have been facilitated along the vessels. Nevertheless, information on the tumor microenvironment is gained by these revelations: Tumor angiogenesis is one of the most significant factors of tumor progression, and several studies link high microvessel density with more advanced tumor stages and poor prognosis [28]. From the images obtained with the described methods, both fibrotic collagen tissue (dense fibers sharing the same orientation e.g. in Fig. 10(d)) and dense vascular networks (Fig. 10(f)) can be spotted and quantified for further analysis. To detect those ROI, SLOT measurements can be used to provide an overview of the general collagen and vascular distribution. The two methods can therefore be used complementary to get a more complete picture of the collagen network (SHG) and tumor microenvironment.

5. Conclusion and outlook

This work demonstrates methods and protocols to enable the analysis of the tumorous microenvironment on different size scales and with varying levels of detail and specificity. The marker-free SHG projections provide a genuine depiction of the collagen network and can be incorporated into standard procedure such as antibody staining to provide complementary information. The advantages of SLOT lie in the high flexibility regarding the sample choice and information obtained. Further optimization of the protocols and for staining and reconstruction will reveal the true power of light-based tomography for imaging of the tumor architecture. In addition, the examination of healthy breast tissue with SHG-SLOT would be desirable. Insights gained from comprehensive imaging studies shall be helpful to determine the role of the tumor microenvironment during cancer progression and treatment.

Disclosures. The authors declare no conflicts of interest.

Data availability. Data underlying the results presented in this paper are not publicly available but may be obtained from the authors upon reasonable request.

References

1. K. Aysola, A. Desai, C. Welch, J. Xu, Y. Qin, V. Reddy, R. Matthews, C. Owens, J. Okoli, D. J. Beech, C. J. Piyathilake, S. P. Reddy, and V. N. Rao, "Triple negative breast cancer–an overview," Hereditary Genet. **2013**(Suppl 2), 001 (2012).
2. T. Oskarsson, "Extracellular matrix components in breast cancer progression and metastasis," The Breast **22**, S66–S72 (2013).
3. T. R. Cox and J. T. Erler, "Remodeling and homeostasis of the extracellular matrix: implications for fibrotic diseases and cancer," Dis. Models Mech. **4**(2), 165–178 (2011).
4. G. Said, M. Guilbert, H. Morjani, R. Garnotel, P. Jeannesson, and H. El Btaouri, "Extracellular matrix proteins modulate antimigratory and apoptotic effects of doxorubicin," Chemotherapy Res. Practice **2012**, 1–10 (2012).
5. V. G. Abramson and I. A. Mayer, "Molecular heterogeneity of triple-negative breast cancer," Current Breast Cancer Rep. **6**(3), 154–158 (2014).
6. G. Cox and E. Kable, "Second-harmonic imaging of collagen," in *Cell Imaging Techniques* (Springer, 2006), pp. 15–35.
7. D. R. Miller, J. W. Jarrett, A. M. Hassan, and A. K. Dunn, "Deep tissue imaging with multiphoton fluorescence microscopy," Curr. Opinion Biomed. Eng. **4**, 32–39 (2017).
8. B. Wen, K. R. Campbell, K. Tilbury, O. Nadiarnykh, M. A. Brewer, M. Patankar, V. Singh, K. W. Eliceiri, and P. J. Campagnola, "3D texture analysis for classification of second harmonic generation images of human ovarian cancer," Sci. Rep. **6**(1), 35734 (2016).
9. R.-A. Lorbeer, M. Heidrich, C. Lorbeer, D. F. R. Ojeda, G. Bicker, H. Meyer, and A. Heisterkamp, "Highly efficient 3d fluorescence microscopy with a scanning laser optical tomograph," Opt. Express **19**(6), 5419–5430 (2011).

10. L. Nolte, G. C. Antonopoulos, L. Rämisch, A. Heisterkamp, T. Ripken, and H. Meyer, "Enabling second harmonic generation as a contrast mechanism for optical projection tomography (OPT) and scanning laser optical tomography (SLOT)," Biomed. Opt. Express **9**(6), 2627–2639 (2018).

11. F. J. Ávila, O. Del Barco, and J. M. Bueno, "Polarization dependence of aligned collagen tissues imaged with second harmonic generation microscopy," J. Biomed. Opt. **20**(8), 086001 (2015).

12. J. Strietz, S. S. Stepputtis, M. Follo, P. Bronsert, E. Stickeler, and J. Maurer, "Human primary breast cancer stem cells are characterized by epithelial-mesenchymal plasticity," Int. J. Mol. Sci. **22**(4), 1808 (2021).

13. M. Kellner, M. Heidrich, R.-A. Lorbeer, G. C. Antonopoulos, L. Knudsen, C. Wrede, N. Izykowski, R. Grothausmann, D. Jonigk, M. Ochs, T. Ripken, M. P. Kühnel, and H. Meyer, "A combined method for correlative 3d imaging of biological samples from macro to nano scale," Sci. Rep. **6**(1), 1–12 (2016).

14. J. Schindelin, I. Arganda-Carreras, E. Frise, V. Kaynig, M. Longair, T. Pietzsch, S. Preibisch, C. Rueden, S. Saalfeld, B. Schmid, J.-Y. Tinevez, J. D. White, V. Hartenstein, K. Eliceiri, P. Tomancak, and A. Cardona, "Fiji: an open-source platform for biological-image analysis," Nat. Methods **9**(7), 676–682 (2012).

15. S. Preibisch, S. Saalfeld, and P. Tomancak, "Globally optimal stitching of tiled 3d microscopic image acquisitions," Bioinformatics **25**(11), 1463–1465 (2009).

16. J. R. Kremer, D. N. Mastronarde, and J. R. McIntosh, "Computer visualization of three-dimensional image data using imod," J. Struct. Biol. **116**(1), 71–76 (1996).

17. Z. Püspöki, M. Storath, D. Sage, and M. Unser, "Transforms and operators for directional bioimage analysis: a survey," Adv. Anat. Embryol Cell Biol. **219**, 69–93 (2016).

18. A. M. Stein, D. A. Vader, L. M. Jawerth, D. A. Weitz, and L. M. Sander, "An algorithm for extracting the network geometry of three-dimensional collagen gels," J. Microsc. **232**, 463–475 (2008).

19. J. S. Bredfeldt, Y. Liu, C. A. Pehlke, M. W. Conklin, J. M. Szulczewski, D. R. Inman, P. J. Keely, R. D. Nowak, T. R. Mackie, and K. W. Eliceiri, "Computational segmentation of collagen fibers from second-harmonic generation images of breast cancer," J. Biomed. Opt. **19**(1), 016007 (2014).

20. R. Gurrala, C. E. Byrne, L. M. Brown, R. F. P. Tiongco, M. D. Matossian, J. J. Savoie, B. M. Collins-Burow, M. E. Burow, E. C. Martin, and F. H. Lau, "Quantifying breast cancer-driven fiber alignment and collagen deposition in primary human breast tissue," Front. Bioeng. Biotechnol. **9**, 618448 (2021).

21. N. Yayon, A. Dudai, N. Vrieler, O. Amsalem, M. London, and H. Soreq, "Intensify3d: Normalizing signal intensity in large heterogenic image stacks," Sci. Rep. **8**(1), 4311 (2018).

22. I. Arganda-Carreras, V. Kaynig, C. Rueden, K. W. Eliceiri, J. Schindelin, A. Cardona, and H. Sebastian Seung, "Trainable weka segmentation: a machine learning tool for microscopy pixel classification," Bioinformatics **33**(15), 2424–2426 (2017).

23. R. Shkarin, A. Shkarin, S. Shkarina, A. Cecilia, R. A. Surmenev, M. A. Surmeneva, V. Weinhardt, T. Baumbach, and R. Mikut, "Quanfima: An open source python package for automated fiber analysis of biomaterials," PLoS One **14**(4), e0215137 (2019).

24. J. Xu and G.-P. Shi, "Vascular wall extracellular matrix proteins and vascular diseases," Biochimica et Biophys. Acta (BBA) - Mol. Basis Dis. **1842**(11), 2106–2119 (2014).

25. B. L. Cox, B. Wen, E. M. Shelton, K. Eliceiri, K. R. Campbell, P. J. Campagnola, and R. Swader, "3D second harmonic generation imaging tomography by multi-view excitation," Optica **4**(10), 1171–1179 (2017).

26. L. Mostaço-Guidolin, N. L. Rosin, and T.-L. Hackett, "Imaging collagen in scar tissue: developments in second harmonic generation microscopy for biomedical applications," Int. J. Molecular Sci. **18**(8), 1772 (2017).

27. S. Ranjit, A. Dvornikov, M. Stakic, S.-H. Hong, M. Levi, R. M. Evans, and E. Gratton, "Imaging fibrosis and separating collagens using second harmonic generation and phasor approach to fluorescence lifetime imaging," Sci. Rep. **5**(1), 13378 (2015).

28. M. A. Senchukova, N. V. Nikitenko, O. N. Tomchuk, N. V. Zaitsev, and A. A. Stadnikov, "Different types of tumor vessels in breast cancer: morphology and clinical value," SpringerPlus **4**(1), 512 (2015).

29. H. Kamin, L. Nolte, J. Maurer, A. Bleilevens, E. Stickeler, S. Johannsmeier, D. Heinemann, and T. Ripken, "Quantification of collagen networks in mammary tumors using tpef and laser-based tomography," Proc. SPIE **11966**, 119660B (2022).

30. H. Kamin, L. Nolte, J. Maurer, A. Bleilevens, E. Stickeler, S. Johannsmeier, D. Heinemann, and T. Ripken, "3d-imaging and quantification of collagen networks in mammary tumors on different size scales," in *Proceedings of the European Conferences on Biomedical Optics 2021 (ECBO)* (OSA Technical Digest (Optica Publishing Group, 2021), p. paper ETu4B.3.